

# Resting-state functional MRI signal fluctuation amplitudes are correlated with brain amyloid- $\beta$ deposition in patients with mild cognitive impairment

Norman Scheel<sup>1</sup> , Takashi Tarumi<sup>2,3</sup>, Tsubasa Tomoto<sup>2,4</sup> ,  
 C Munro Cullum<sup>4,5,6</sup>, Rong Zhang<sup>2,4</sup> and David C Zhu<sup>1</sup>

## Abstract

Mounting evidence suggests that amyloid- $\beta$  (A $\beta$ ) and vascular etiologies are intertwined in the pathogenesis of Alzheimer's disease (AD). Blood-oxygen-level-dependent (BOLD) signals, measured by resting-state functional MRI (rs-fMRI), are associated with neuronal activity and cerebrovascular hemodynamics. Nevertheless, it is unclear if BOLD fluctuations are associated with A $\beta$  deposition in individuals at high risk of AD. Thirty-three patients with amnesic mild cognitive impairment underwent rs-fMRI and AV45 PET. The AV45 standardized uptake value ratio (AV45-SUVR) was calculated using cerebral white matter as reference, to assess A $\beta$  deposition. The whole-brain normalized amplitudes of low-frequency fluctuations (sALFF) of local BOLD signals were calculated in the frequency band of 0.01–0.08 Hz. Stepwise increasing physiological/vascular signal regressions on the rs-fMRI data examined whether sALFF-AV45 correlations were driven by vascular hemodynamics, neuronal activities, or both. We found that sALFF and AV45-SUVR were negatively correlated in regions of default-mode and visual networks (precuneus, angular, lingual and fusiform gyri). Regions with higher sALFF had less A $\beta$  accumulation. Correlated cluster sizes in MNI space ( $r \approx -0.47$ ) were reduced from 3018 mm<sup>3</sup> to 1072 mm<sup>3</sup> with stronger cardiovascular regression. These preliminary findings imply that local brain blood fluctuations due to vascular hemodynamics or neuronal activity can affect A $\beta$  homeostasis.

## Keywords

ALFF, amyloid- $\beta$ , AV45, PET, resting-state fMRI

Received 30 April 2021; Revised 15 October 2021; Accepted 15 November 2021

## Introduction

Alzheimer's disease (AD) is a major neurodegenerative brain disorder and the most common type of dementia among older adults.<sup>1</sup> Patients with AD exhibit memory loss, impaired decision-making capacity, disorientation, as well as changes in daily functional abilities.<sup>2</sup> These cognitive deficits and behavioral changes are accompanied and often preceded by brain pathophysiological changes including amyloid- $\beta$  (A $\beta$ ) and tau protein depositions in the cerebral cortex, brain hypoperfusion, and neuronal degeneration.<sup>3</sup> Mild cognitive impairment (MCI), particularly amnesic mild cognitive impairment (aMCI), has been considered to represent a transitional phase between normal cognitive aging and AD, as many who develop aMCI progress to AD.<sup>4</sup>

<sup>1</sup>Department of Radiology and Cognitive Imaging Research Center, Michigan State University, East Lansing, MI, USA

<sup>2</sup>Institute for Exercise and Environmental Medicine, Texas Health Presbyterian Hospital, Dallas, TX, USA

<sup>3</sup>Human Informatics and Interaction Research Institute, National Institute of Advanced Industrial Science and Technology, Tsukuba, Ibaraki, Japan

<sup>4</sup>Department of Neurology, University of Texas Southwestern Medical Center, Dallas, TX, USA

<sup>5</sup>Department of Psychiatry, University of Texas Southwestern Medical Center, Dallas, TX, USA

<sup>6</sup>Department of Neurological Surgery, University of Texas Southwestern Medical Center, Dallas, TX, USA

## Corresponding authors:

David C Zhu, Department of Radiology, Michigan State University, 846 Service Road, East Lansing, MI 48824, USA.  
 Email: zhuda@msu.edu

Rong Zhang, Department of Neurology, University of Texas Southwestern Medical Center, 7232 Greenville Ave, Dallas, TX 75231, USA.

Email: RongZhang@TexasHealth.org

Two major hypotheses have been developed to understand the pathophysiological mechanisms of AD and to develop effective treatments. In the classic amyloid cascade hypothesis, the disruption of brain A $\beta$  homeostasis has been proposed to be a primary driver of AD, leading to accumulations of A $\beta$  plaques and neurofibrillary tangles, and consequently neurodegeneration and cognitive impairment.<sup>5</sup> Conversely, the vascular hypothesis of AD proposes that cerebrovascular dysfunction is an important contributor to AD onset and progression.<sup>6–8</sup> Mounting evidence indicates that A $\beta$  and vascular factors are intertwined in the pathogenesis of AD.<sup>9,10</sup> In a recent study, we found that age-related carotid artery stiffness was associated positively with brain A $\beta$  burden in aMCI patients, supporting the role of arterial aging in brain A $\beta$  deposition.<sup>11</sup> Recent animal and human studies also suggest that cerebral arterial oscillations and vasomotions influence brain A $\beta$  clearance and deposition.<sup>12–14</sup>

Spontaneous cerebral blood flow (CBF) fluctuations are linked intrinsically to brain neuronal activities through neurovascular coupling.<sup>15–17</sup> This phenomenon has been exploited by using resting-state functional MRI (rs-fMRI) to understand functional connectivities between brain regions and the disruption of functional connectivity in diseased states.<sup>16,18–26</sup> Specifically, it has been proposed that spontaneous neuronal activities, which consume approximately 95% of the brain's metabolism,<sup>16</sup> are manifested as rs-fMRI blood-oxygen-level-dependent (BOLD) signal fluctuations.<sup>16,17,27</sup>

It has been widely recognized that spontaneous BOLD fluctuations are influenced by both systemic and cerebrovascular hemodynamics in addition to neuronal activities.<sup>28–32</sup> Rajna et al. recently applied a 3D multi-resolution optical flow analysis technique and showed that the cardiovascular pulse propagates from major arteries via cerebral spinal fluid spaces into all tissue compartments in the brain and found that cardiovascular pulsations were significantly altered in AD.<sup>33,34</sup> In this regard, our previous work has shown that spontaneous fluctuations of BOLD signals and CBF velocity measured in the middle cerebral artery (upper-stream vascular signals) had similar spectral distributions and high correlation in the 0.01–0.08 Hz frequency band.<sup>35</sup> These observations suggested that upper-stream cerebrovascular hemodynamic fluctuations can transmit downstream into the cerebral microcirculation and contribute importantly to regional BOLD fluctuations. On the other hand, local cerebral vasomotion, which has been linked to brain A $\beta$  clearance, also may influence rs-fMRI BOLD fluctuations.<sup>12</sup>

An early study investigating the relationship of BOLD signals and amyloid deposition suggests that high levels of amyloid deposition are associated with

an altered fMRI default-mode network % signal change in a memory encoding task paradigm in asymptomatic and minimally impaired older individuals.<sup>36</sup> Based on the data from the Alzheimer's Disease Neuroimaging Initiative's (ADNI), another study found that physiological fluctuations in white matter (based on rs-fMRI BOLD signal standard deviations) increased in AD and that this increase was associated with a decrease in regional glucose metabolism measured by FDG-PET in the default-mode network areas.<sup>37</sup> In a small ADNI subgroup, a greater BOLD signal variability, measured by the temporal standard deviation of rs-fMRI voxel time courses, was found in white and gray matter regions involving the default-mode network in AD patients.<sup>38</sup> A recent study employing data from ADNI supplemented with high-temporal-resolution rs-fMRI data with a repetition time (TR) of 0.1 s showed an increased fMRI signal variability at cardiorespiratory frequencies in AD patients when compared to cognitively normal performing older adults.<sup>39</sup> In sum, these findings suggest a possible link among BOLD signal variability, upper-stream cardiovascular effects, regional brain metabolic activity and AD. As A $\beta$  plaques are a major hallmark of AD, it is crucial to understand possible effects of BOLD signal variability on brain A $\beta$  deposition. In this study, we investigated the correlation on voxel basis between rs-fMRI BOLD signal fluctuation amplitude and A $\beta$  deposition from AV45-PET amyloid imaging in aMCI patients. BOLD signal fluctuations in this study were quantified by the amplitude of low-frequency fluctuations (ALFF)<sup>40</sup> which is based on the power spectrum within the specific frequency range of neurovascular activity, rather than temporal BOLD standard deviations from the mean. Furthermore, we examined whether the associations between local ALFF and brain A $\beta$  depositions are influenced by upper-stream cerebrovascular hemodynamics, spontaneous neuronal activities or both, using differential signal regression approaches.<sup>41–43</sup> We hypothesized that local ALFF would be negatively correlated with brain A $\beta$  deposition and that correlation strength between ALFF and A $\beta$  deposition would decrease when the upper-stream vascular signals are regressed out from the raw BOLD signal under an assumption that upper-stream vascular effects drive brain A $\beta$  clearance.

## Material and methods

### Participants

Thirty-three aMCI subjects ( $64.4 \pm 6.4$  years of age, 19 females) were recruited who represent a subgroup of participants enrolled in a proof of concept

investigation aimed to identify effects of exercise training on neurocognitive function in aMCI subjects (ClinicalTrials.gov, NCT01146717).<sup>44</sup> Data presented here were obtained at baseline before any intervention. The diagnosis of aMCI was based on the Petersen criteria as modified by the ADNI project (<http://adni-info.org>).<sup>45</sup> Diagnostic assessments included the Clinical Dementia Rating (CDR) scale,<sup>46</sup> the Mini-Mental State Examination (MMSE),<sup>47</sup> and the Wechsler Memory Scale-Revised Logical Memory (LM) immediate and delayed recall trials.<sup>48</sup> Heart rate (HR) and brachial cuff blood pressure (BP) were measured >3 times with an ECG-gated electro-sphygmomanometer (Suntech, Morrisville, NC, USA). Obtained values were averaged to obtain HR, systolic (SBP), and diastolic BP (DBP). Participants with major psychiatric disorders, major or unstable medical conditions, uncontrolled hypertension, diabetes mellitus, or chronic inflammatory diseases were excluded, as were participants with implants or other issues preventing them from undergoing MRI scanning (details are provided in ClinicalTrials.gov NCT01146717). All participants gave informed consent. This study was approved by the Institutional Review Boards of the University of Texas Southwestern Medical Center and Texas Health Presbyterian Hospital of Dallas and performed by the guidelines of the Declaration of Helsinki and Belmont Report.

### MRI measurements

Rs-fMRI data were collected on a Philips Achieva 3T scanner (Philips Healthcare, Best, the Netherlands) under an “Eye-closed” condition with the following parameters: gradient recalled echo planner imaging (EPI), 29 contiguous 5-mm axial slices, 30-ms time of echo (TE), 1500-ms time of repetition (TR), 60° flip angle, a 24-cm field of view, 80 × 80 matrix size and 200 time-points. High-resolution T<sub>1</sub>-weighted 3D MPRAGE (Magnetization-Prepared Rapid Acquisition Gradient-Echo) images were also collected to cover the whole brain with the following parameters: TE/TR = 3.7/8.1 ms, flip angle = 12°, field of view = 256 mm × 204 mm, 160 1-mm slices, resolution = 1 mm × 1 mm × 1 mm, SENSE factor = 2 and scan duration = 4 minutes.

### PET image acquisition

After an intravenous bolus injection of 10 mCi <sup>18</sup>F-florbetapir (also called AV45), participants were positioned in a Siemens (Munich, Germany) ECAT HR PET scanner for data acquisition, using laser guidance for precise head positioning. A 2-minute scout scan was acquired first. At 50 minutes post-injection, 2 frames of 5-minute PET emission scan and a 7-minute

transmission scan were acquired in 3D mode using the following parameters: matrix size = 128 × 128, resolution = 5 mm × 5 mm, slice thickness = 2.42 mm, and field of view = 58.3 cm. Emission images were processed with four iterative reconstructions and 16 subsets with a 3-mm full width at half maximum (FWHM) ramp filter. The transmission image was reconstructed using back-projection and a 6-mm FWHM Gaussian filter for attenuation correction.<sup>49,50</sup>

### RS-fMRI BOLD signal fluctuation quantification

The quantification of rs-fMRI BOLD local signal fluctuation using ALFF was first proposed by Zang et al.<sup>40</sup> to investigate rs-fMRI signal fluctuations in attention deficit hyperactivity disorder. To calculate ALFF, rs-fMRI recordings are first pre-processed, including slice-timing correction, motion correction, and spatial blurring (different strategies used are detailed later). No temporal filtering is applied before ALFF calculation. Fast Fourier transformation (FFT) is carried out on each preprocessed voxel time course. The ALFF index is calculated as two times the amplitude of the FFT output, divided by the sample length (number of data points in the time course), then averaged across the specified frequency band of interest.

A frequency band of 0.01–0.08 Hz was used in this study. Figure 1(a) shows a typical pre-processed rs-fMRI time course at a brain voxel. Figure 1(b) shows the corresponding Fourier spectrum and the frequency band for ALFF computation. ALFF at each voxel is subsequently normalized by the global mean ALFF from all voxels within the brain to generate a standardized ALFF (sALFF) index, which was then used to compare across subjects and different regression procedures. ALFF computations were carried out using the ALFF function included in the DPARSFA toolbox from the “DPABI V4.3\_200401” software package<sup>51,52</sup> in MATLAB R2019a (MathWorks, Natick, MA, USA).

### Anatomical image pre-processing and MNI-registration

One common challenge in brain imaging studies of older adults is the high degree of anatomical variability due to atrophy, leading to difficulties in performing group-wise image analyses. FreeSurfer,<sup>53</sup> a software for cortical surface reconstruction and anatomical brain MRI segmentation, provides a robust segmentation in comparable study cohorts, as demonstrated in a prior AD imaging study.<sup>26</sup> The high-resolution T<sub>1</sub>-weighted volumetric MR images of each participant were processed using the FreeSurfer “recon-all” pipeline. This pipeline creates a non-linear transformation

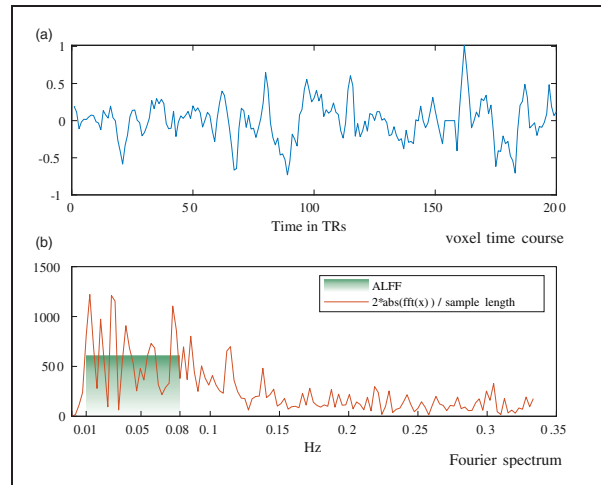


**Figure 1.** Time series and spectral analysis of spontaneous BOLD signal fluctuations (a) time course at a voxel in the occipital region of one study participant; (b) corresponding Fourier spectrum. Across the applied frequency band of 0.01–0.08 Hz, the amplitude of low-frequency fluctuations (ALFF) yields 605.7 as of this voxel's fluctuation amplitude (plotted in the green shade).

matrix that warps images from a participant's native space to MNI standard space, according to the MNI305 template resolution ( $1\text{ mm} \times 1\text{ mm} \times 1\text{ mm}$  with a matrix size of  $256 \times 256 \times 256$ ). This transformation matrix was applied to warp the results of the sALFF and AV45 calculations to the MNI305 template. Visual assessment revealed that the transformation to the standard template performed well overall for all brains. Subsequently, for computational efficiency, all images in MNI305 template resolution were resampled to fit the MNI152 template with a resolution of  $2\text{ mm} \times 2\text{ mm} \times 2\text{ mm}$  at a matrix size of  $91 \times 109 \times 91$ .

### fMRI preprocessing and physiological/vascular signal regression

Resting-state fMRI pre-processing was first carried using AFNI<sup>54</sup> in native space. The “afni\_proc.py” routine in AFNI was used to generate the script to preprocess the rs-fMRI data. For each participant, signal spikes in the signal intensity time courses were first detected and removed. The acquisition timing difference was then corrected for different slice locations. With the third functional volume as the reference, rigid-body motion correction was carried out in three translational and three rotational directions. The displacements due to motion in these six directions as well as the corresponding motion derivatives were estimated and modeled as motion regressors. Data points with excess motion (normalized motion derivative  $>0.5$  or voxel outliers  $>10\%$ ) were identified to generate additional motion regressors. System induced trends up to the 3rd order were also modeled as regressors. Spatial blurring with a full width half maximum (FWHM) of

4mm was used to reduce random noise. AFNI's “3dDeconvolve” function was applied to remove the motion and system introduced noises through the regressors described above. Up to this step, physiological signals, including upper-stream vascular effects, remained in the signal. The resulting fMRI dataset up to this step will be called “No physiological regression” to emphasize that no attempt has been made to remove upper-stream vascular effects.

The standardized amplitude of the BOLD signal fluctuations (sALFF) within the frequency range of 0.01 Hz to 0.08 Hz was then calculated for each voxel within the brain. For group analyses, subject-space sALFF maps were non-linearly transformed into MNI305 standard space, using the transformation matrix created by the FreeSurfer processing pipeline as discussed above. MNI305 sALFF images were subsequently resampled to fit the MNI152 standard template. The correlation between sALFF and brain amyloid  $\beta$  accumulation, calculated as AV45 PET amyloid  $\beta$  standardized uptake value ratio (SUVR), was then calculated in MNI152 standard space as discussed further in the following section. To understand the upper-stream physiological/vascular effects, the “no physiological regression” dataset was further processed with three progressively more aggressive physiological signal regression procedures. For each procedure, sALFF was calculated again followed by the aforementioned standard-space transformations and correlation analyses. The three regression procedures, in addition to the “no physiological regression”, are listed below:

1. “No physiological regression:” as described above, this procedure has no special treatment to remove

- upper-stream physiological/vascular effects before sALFF computation.
2. “WM/CSF regression:” White matter (WM) and cerebrospinal fluid (CSF) do not contain neuronal brain activity. Consequently, fluctuations of mean BOLD signal time courses at these regions can be assumed to mostly represent upper-stream vascular effects.<sup>55</sup> Hence, CSF and WM signals were modeled and used as additional regressors in the “3dDeconvolve” step to reduce the upper-stream vascular influence, before sALFF computation.
  3. “WM/CSF/GS regression:” The mean global signal (GS) was assumed to be primarily driven by an overall upper-stream vascular effect and added as an additional regressor to this “WM/CSF regression” procedure for further physiological signal removal before sALFF computation. With this procedure, the resulting signal time course should closely reflect neuronal brain activity.<sup>55</sup> While global signal removal can potentially remove some neuronal signals from fMRI data, current research suggests that the upper-stream vascular components most likely dominate the global signal.<sup>56–58</sup> Recently, Xifra-Porxas and colleagues reported that physiological signals accounted for an  $r$  of about 0.6 within the global signal.<sup>56</sup> Here, global signal regression was used to further investigate the effect of the upper-stream vascular signals on  $A\beta$  deposition in the brain and its influence in this cascaded setup.
  4. “Aggressive AROMA:” A rs-fMRI denoising technique called “ICA-AROMA” was developed by Pruim and colleagues<sup>41</sup> to aggressively remove motion artifacts and physiological noise. The authors demonstrated that this technique could effectively identify motion and physiological signals as independent components and then remove them from rs-fMRI data.<sup>59</sup> “ICA-AROMA” was implemented using FSL’s MELODIC routine<sup>60</sup> where single-subject spatial independent component analysis (ICA) is performed on a motion-corrected whole-brain rs-fMRI dataset in native space. Using a pre-trained classifier, the resulting components are sorted into noise and non-noise components. The time courses of components identified as noise are subsequently regressed from the data using FSL’s “regfilt” function, where partial regression is called “non-aggressive AROMA,” and full regression is called “aggressive AROMA.” The “aggressive AROMA” approach was employed here to maximize the effect of removing upper-stream vascular signals.

The overall signal processing steps described above are also presented in supplementary Figure S1.

### PET image processing

Using “flirt” from the FSL software package,<sup>60</sup> a six-degree linear transformation was applied to align PET AV45-SUVR images to the 3D MPRAGE anatomical MRI images. All alignments were visually inspected and improved with manual adjustments if necessary. Using the segmentation of the high-resolution 3D MPRAGE image from the FreeSurfer analysis, white-matter (WM) and cerebellar regions were isolated. An additional erosion of the WM map, using FSL’s “fslmaths” with a box kernel of  $4\text{ mm} \times 4\text{ mm} \times 4\text{ mm}$  ensured that only WM regions were obtained. The AV45 uptake images were then normalized by the mean uptake at the WM and also the cerebellar regions to generate two versions of SUVR images. Previous studies have shown that SUVR calculation using WM signal can improve discriminatory power for detecting AD and MCI.<sup>61</sup> In the following, SUVR will be reported for WM normalization, yet post-hoc analyses with the AV45-SUVR images normalized by cerebellar signal were also carried out to confirm observations. Congruent to the spatial normalization of sALFF maps, AV45-SUVR images were non-linearly transformed to match the MNI305 standard template, using the transformation matrix created by the FreeSurfer processing pipeline. AV45-SUVR images in MNI305 template space were subsequently resampled to fit the MNI152 standard template.

### Statistical analysis

All quantitative measures are reported as mean  $\pm$  standard deviation. For all statistical tests, data normality was assessed using Kolmogorov-Smirnov tests, and non-parametric testing was employed if data was not normally distributed. Correlations between sALFF and AV45-SUVR across participants were carried out for each brain voxel in MNI152 template space. Monte-Carlo simulations, using 10,000 random permutations for each correlation value  $r$ , were applied to approximate the corresponding  $p$  values, through constructing voxel-specific empirical cumulative distributions,<sup>62</sup> in MATLAB R2019a (MathWorks, Natick, MA, USA). Cluster-level multiple-comparison corrections were computed using AFNI’s<sup>54</sup> “3dClustSim” Monte-Carlo simulation. In these simulations, we estimated the minimum cluster sizes required to achieve a corrected  $p \leq 0.05$  at a voxel-level  $p < 0.001$ . As the estimated minimum cluster size is highly dependent on data spatial smoothness, which in turn depends on data preprocessing, cluster size thresholds were estimated independently for each physiological/vascular signal removal procedure, described earlier. Autocorrelation function parameters (-acf) employed by “3dClustSim”

were estimated using “3dFWHMx” (AFNI) on the pre-processed fMRI data in MNI152 template space. This procedure yields mean parameters (across participants) for each of the four different autocorrelation functions, specific to each fMRI preprocessing procedure. We also estimated the spatial autocorrelation of the AV45-SUVR maps using “3dFWHMx”. Our pre-processed fMRI images showed less auto-correlation than the AV45-SUVR maps. To be conservative, we used the autocorrelation estimates of the fMRI images to calculate the required cluster sizes to achieve statistical significance. Subsequently, “3dClusterize” (AFNI) was used to generate correlation cluster maps that survive the estimated cluster correction thresholds for each preprocessing procedure.

The preprocessing-specific significant clusters were then used to assess whether the correlations between BOLD signal fluctuations and brain amyloid deposition were rather influenced by upper-stream physiological/vascular effects or neuronal activations. For this purpose, we illustrated the distributions of the Fisher  $z$  transformed  $r$  values of the AV45-SUVR-sALFF correlations, using the voxel populations identified as significant clusters resulting from the analyses based on the “no physiological regression” and the “aggressive AROMA” procedures.

To provide an additional insight on the relationship between sALFF and AV45-SUVR from a within-brain perspective, we used the anatomical brain parcellation of the AAL atlas<sup>63</sup> to calculate the mean sALFF and mean AV45-SUVR within each of the 116 grey matter regions spanning the whole brain. The correlation between sALFF and AV45-SUVR across the regions within the brain results in one  $r$  value per subject for each regression procedure, representing the within-brain internal association between sALFF and AV45-SUVR. Then on the Fisher- $z$  transformed  $r$  values, Wilcoxon signed rank tests were performed to inform about the effects of the regression procedures and a Kruskal-Wallis test was performed to inform about the overall differential effects of the regression procedures on the correlation between sALFF and AV45-SUVR.

## Results

Table 1 shows the participant characteristics. Overall, our aMCI patients were well educated and showed early aMCI symptoms, as shown by CDR scores of 0.5, a mean MMSE score of  $29.5 \pm 0.8$ , and mean LM immediate recall of  $11.4 \pm 2.3$  and delayed recall of  $9.7 \pm 1.8$ . These older adults had an average heart rate of 62 bpm and mean systolic blood pressure of 118 mmHg but included hypertension ( $\geq 140$  mmHg). The presence of apolipoprotein E4 (APOE4) was

assessed in 28 participants and 25% were APOE4 positive. The participants had a mean cortical AV45-SUVR of  $0.57 \pm 0.05$  when normalized with the white matter as a reference and  $1.15 \pm 0.08$  with the whole cerebellum as a reference.

Figures 2 and S6 show graphical representations of select sagittal and axial slices of mean AV45-SUVR, mean sALFF for each preprocessing procedure, and the significant correlation clusters between them. Table 2 provides a detailed list of significant correlation clusters with associated brain regions for each preprocessing procedure. Using the “no physiological regression” procedure, cluster level significance was estimated with voxel-level  $p < 0.001$  and a corrected  $p \leq 0.05$ , yielding a minimum cluster size requirement of 493 voxels (2-mm isotropic). Using this threshold, four significant negatively correlated clusters between sALFF and AV45-SUVR were found spanning across the lingual gyrus, precuneus, cuneus, and fusiform gyrus, with the most prominent cluster reaching a size of approximately  $3018 \text{ mm}^3$  (see Table 2, Figures 2b & S6b).

After applying the “WM/CSF regression” procedure using the same statistical criteria as above, the corrected  $p \leq 0.05$  was achieved with a minimum cluster size of 434 voxels. At this threshold, four clusters were identified as significant. The significant brain regions are consistent with the “no physiological regression” methods, spanning the lingual gyrus, fusiform gyri, cuneus, and precuneus, yet at slightly smaller cluster

**Table 1.** Participant characteristics.

	Mean $\pm$ SD	Minimum	Maximum
Men/women (n)		14/19	
Race (n)		29 Caucasian, 4 African American	
APOE4 carrier, <sup>a</sup> n (%)		7 (25%)	
Age (years)	$64 \pm 7$	55	78
Height (cm)	$169 \pm 9$	143	184
Body mass (kg)	$79 \pm 14$	58	117
Body mass index ( $\text{kg}/\text{m}^2$ )	$28 \pm 4$	21	36
Education (years)	$16 \pm 2$	12	18
Clinical Dementia Rating (points)		0.5	
MMSE total	$29.5 \pm 0.8$	27	30
Logical Memory immediate recall	$11.4 \pm 2.3$	5	16
Logical Memory delayed recall	$9.7 \pm 1.8$	6	15
Heart rate (bpm)	$62 \pm 9$	44	81
Systolic blood pressure (mmHg)	$118 \pm 18$	85	152
Diastolic blood pressure (mmHg)	$70 \pm 8$	53	87

<sup>a</sup>Apolipoprotein E4 (APOE4) was assessed in 28 patients.

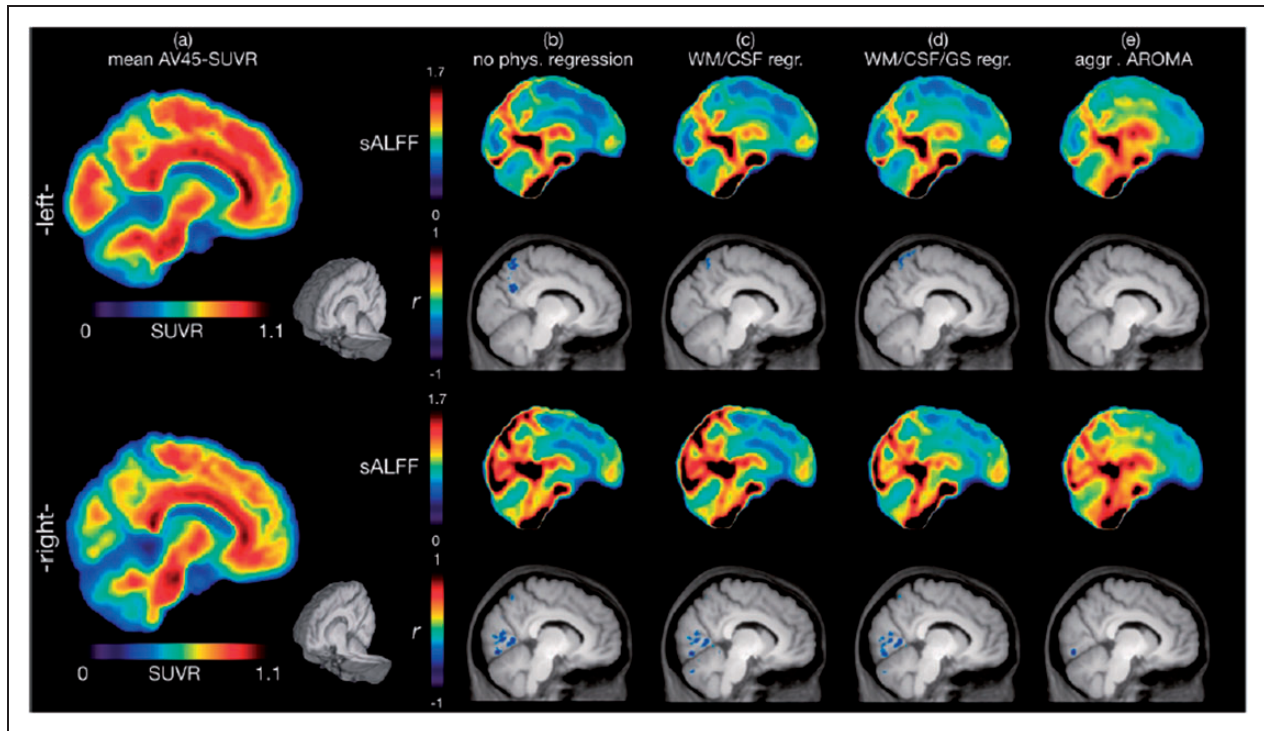


**Figure 2.** Voxel-wise correlation analysis between brain amyloid- $\beta$  deposition and the standardized amplitude of low-frequency BOLD signal fluctuations (sALFF). Images represent slices near the mid-sagittal region (right and left 9.25 mm in MNI space). (a) mean AV45-SUVR (standardized uptake value ratio with the white matter as a scaling reference) color maps of 33 amnesic mild cognitive impairment participants are shown along with the corresponding mean sALFF (standardized amplitude of low-frequency fluctuations) color maps after the physiological signal cleaning procedures of (b) “no physiological regression”, (c) “WM/CSF regression”, (d) “WM/CSF/GS regression” and (e) “aggressive AROMA”. Significant correlation clusters between AV45-SUVR and sALFF for each regression procedure (b)-(e) are shown in the row below the mean sALFF images. Clusters are depicted in blue, as  $r$  values are negative (see Table 2 for detailed statistical analysis data). AV45-SUVR maps are nearly identical if the cerebellum, instead of white matter, is used as a reference, except the color scale range becomes 0 to 2. As more global variance is removed with each regression step, the normalization of sALFF reveals local signal oscillations.

sizes for all except the lingual gyrus cluster which slightly increases in size (see Table 2, Figures 2(c) and S6c).

After applying the “WM/CSF/GS regression” procedure using the same statistical criteria as above, the corrected  $p \leq 0.05$  was achieved with a minimum cluster size of 344 voxels. Again, four clusters were identified as significant at brain regions consistent with the prior procedures. While the cluster at the right lingual gyrus, fusiform gyrus, and cuneus increases in size once more, clusters at regions involving precuneus and left fusiform gyrus show smaller cluster sizes (see Table 2, Figures 2(d) and S6d).

After applying the “aggressive AROMA” procedure using the same statistical criteria as above, the corrected  $p \leq 0.05$  was achieved with a minimum cluster size of 384 voxels. Two clusters spanning precuneus, cuneus, angular gyrus, fusiform gyrus, and lingual gyrus were identified as significant, with the most prominent cluster reaching a size of approximately  $1072 \text{ mm}^3$  (see Table 2, Figures 2(e) and S6e).

Overall, significant negative correlations were found between sALFF and AV45-SUVR with all four regression procedures, decreasing in cluster sizes in a stepwise manner based on the aggressiveness of physiological/vascular signal removal. Scatterplots, demonstrating the negative correlation between the mean sALFF and mean AV45-SUVR at the location of the most significant cluster, found using the “no physiological regression” procedure, are depicted in Figure 3, across the four regression procedures. The corresponding scatterplots for all significant voxel populations across all regression procedures are presented in Supplementary Figures S2–S5.

To further understand the effect of the different physiological/vascular signal regression procedures on sALFF and AV45-SUVR correlations, the Fisher  $z$  transformed  $r$ -value distributions at significant voxel locations were illustrated in Figure 4. Using all significant voxel locations for either the “no physiological regression” procedure (4563 voxels) or the “aggressive AROMA” procedure (944 voxels),  $r$ -value distributions

**Table 2.** Correlation cluster analysis of sALFF and AV45-SUVR.

	Cluster-ID	Associated brain regions	Cluster size <sup>a</sup>	Mean $r \pm SD$	Max $r$	MNI coordinates <sup>b</sup>		
						RL	AP	IS
No physiological regression	#1	Right Lingual Gyrus, Right Declive, Right Fusiform Gyrus, Right Middle Occipital Gyrus, Right Inferior Occipital Gyrus, Right Cuneus, Right Culmen	1509	$-0.47 \pm 0.06$	-0.68	-24	52	2
	#2	Right Inferior Parietal Lobule, Right Precuneus, Right Superior Parietal Lobule, Right Superior Temporal Gyrus, Right Supramarginal Gyrus, Right Middle Temporal Gyrus	1432	$-0.48 \pm 0.07$	-0.74	-30	50	38
	#3	Left Precuneus, Left Superior Parietal Lobule, Left Inferior Parietal Lobule, Left Middle Temporal Gyrus	837	$-0.47 \pm 0.06$	-0.72	10	62	26
	#4	Left Fusiform Gyrus, Left Middle Occipital Gyrus, Left Middle Temporal Gyrus, Left Declive, Left Inferior Occipital Gyrus	785	$-0.47 \pm 0.06$	-0.67	28	90	-16
WM/CSF regression	#1	Right Lingual Gyrus, Right Declive, Right Fusiform Gyrus, Right Middle Occipital Gyrus, Right Cuneus, Right Culmen, Right Inferior Occipital Gyrus	1538	$-0.46 \pm 0.05$	-0.66	-8	80	-14
	#2	Left Middle Occipital Gyrus, Left Fusiform Gyrus, Left Declive, Left Middle Temporal Gyrus, Left Inferior Occipital Gyrus	1070	$-0.47 \pm 0.06$	-0.72	28	90	-16
	#3	Left Precuneus, Left Superior Parietal Lobule, Left Inferior Parietal Lobule, Left Supramarginal Gyrus, Left Middle Temporal Gyrus	808	$-0.46 \pm 0.06$	-0.69	38	66	24
	#4	Right Superior Parietal Lobule, Right Precuneus, Right Inferior Parietal Lobule	704	$-0.49 \pm 0.07$	-0.73	-18	62	46
WM/CSF/GS regression	#1	Right Lingual Gyrus, Right Declive, Right Fusiform Gyrus, Right Cuneus, Right Middle Occipital Gyrus, Right Inferior Occipital Gyrus, Right Culmen	1762	$-0.46 \pm 0.05$	-0.67	-22	92	0
	#2	Left Middle Occipital Gyrus, Left Declive, Left Fusiform Gyrus, Left Middle Temporal Gyrus, Left Inferior Occipital Gyrus, Left Uvula	1069	$-0.47 \pm 0.06$	-0.73	28	90	-16
	#3	Right Superior Parietal Lobule, Right Precuneus, Right Inferior Parietal Lobule	567	$-0.47 \pm 0.06$	-0.68	-16	62	56
	#4	Left Superior Parietal Lobule, Left Inferior Parietal Lobule, Left Precuneus	356	$-0.47 \pm 0.06$	-0.69	14	60	64
Aggressive AROMA	#1	Left Precuneus, Left Cuneus, Left Inferior Parietal Lobule, Left Angular Gyrus, Left Middle Temporal Gyrus, Left Superior Parietal Lobule	536	$-0.46 \pm 0.06$	-0.71	38	64	38

(continued)

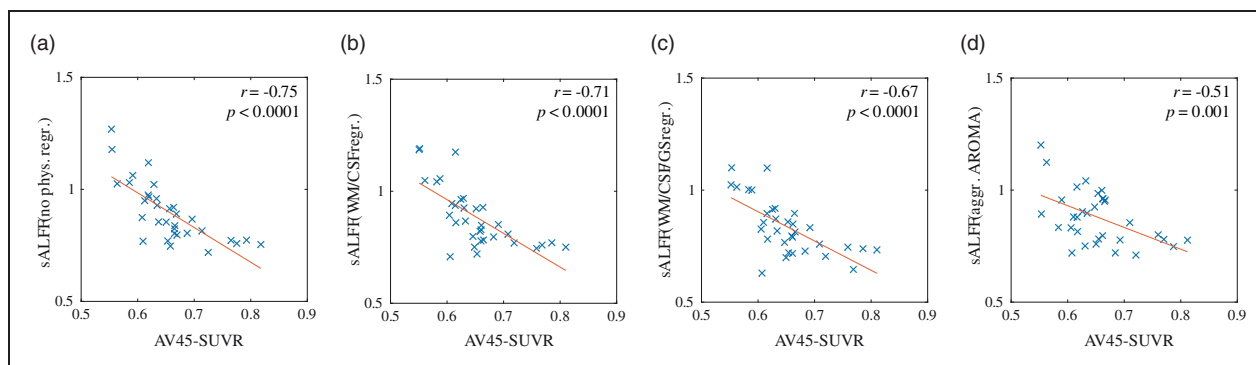


Table 2. Continued.

Cluster-ID	Associated brain regions	Cluster size <sup>a</sup>	Mean $r \pm SD$	Max $r$	MNI coordinates <sup>b</sup>		
					RL	AP	IS
#2	Right Lingual Gyrus, Right Cuneus, Right Declive, Right Inferior Occipital Gyrus, Right Fusiform Gyrus	408	$-0.47 \pm 0.06$	-0.64	-18	74	-8

<sup>a</sup>Cluster size is the number of voxels with a voxel size of  $2 \times 2 \times 2$  mm at a corrected  $p \leq 0.05$ .

<sup>b</sup>MNI coordinates are shown at maximum intensity with RL: right-left; AP: anterior-posterior and IS: inferior-superio.



**Figure 3.** Correlation of brain amyloid- $\beta$  deposition and the amplitude of low-frequency BOLD signal fluctuations (sALFF) for “No physiological regression” Cluster #2 (Table 2). Depicted are scatterplots for each physiological/vascular regression procedure, left to right: (a) “no physiological regression”, (b) “WM/CSF regression”, (c) “WM/CSF/GS regression”, and (e) “aggressive AROMA”. Blue crosses represent the 33 subjects, using mean sALFF and mean AV45 within this cluster. The plots show reduced correlation strength from (a) to (d). Statistical  $p$  values were derived from 10,000 random permutations. For scatterplots of the remaining significant clusters see Supplementary Figures 2–5.

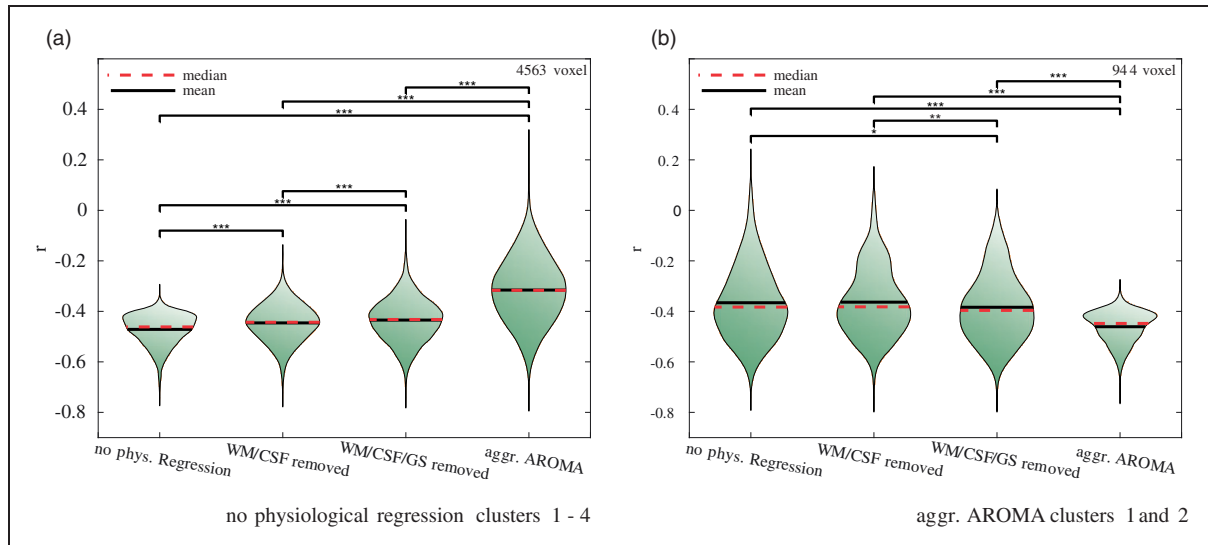
are depicted for each regression procedure at these specific voxel locations. Figure 4 (a) shows the violin plots of the  $r$ -value distributions of significant voxels from the “no physiological regression” procedure with mean and standard deviations as follows:  $-0.47 \pm 0.06$  (“no physiological regression”),  $-0.45 \pm 0.07$  (“WM/CSF regression”),  $-0.43 \pm 0.08$  (“WM/CSF/GS regression”) and  $-0.32 \pm 0.13$  (“aggressive AROMA”). The Kruskal-Wallis test yielded a  $\chi^2 = 3.9 \times 10^3$  with  $p < 0.001$ . All paired Mann-Whitney U-tests were significant.

Figure 4 (b) shows the opposite effect, depicting the violin plots with  $r$ -value distributions of the significant voxel population from the “aggressive AROMA” procedure. The  $r$ -value means and standard deviations at these voxel locations corresponding to each regression procedure are:  $-0.37 \pm 0.14$  (“no physiological regression”),  $-0.36 \pm 0.13$  (“WM/CSF regression”),  $-0.38 \pm 0.13$  (“WM/CSF/GS regression”) and  $-0.46 \pm 0.06$  (“aggressive AROMA”). The Kruskal-Wallis test yielded a  $\chi^2 = 3.11 \times 10^2$  with  $p < 0.001$ . All paired Mann-Whitney U-tests were significant except the one between “no physiological regression” and “WM/CSF regression”.

For the AAL atlas-based analyses across brain regions, the mean Fisher- $z$  transformed correlation between sALFF and AV45-SUVR within the brain for the “no physiological regression” procedure is  $r = -0.28 \pm 0.12$  ( $z = -5$ ,  $p < 0.001$ ), for the “WM/CSF regression” procedure  $r = -0.20 \pm 0.11$  ( $z = -5$ ,  $p < 0.001$ ), for the “WM/CSF/GS regression” procedure  $r = -0.19 \pm 0.09$  ( $z = -5$ ,  $p < 0.001$ ) and for the “aggressive AROMA” procedure  $r = -0.11 \pm 0.13$  ( $z = -3.6$ ,  $p < 0.001$ ). The Kruskal-Wallis test across regression procedures yielded a significant  $\chi^2$  of 25.94 ( $p < 0.001$ ). All paired Mann-Whitney U-tests were significant except the one between “WM/CSF regression” and “WM/CSF/GS regression”. See Figure S7 for details.

## Discussion

The main finding of this study is the observation of significant negative correlations between the sALFF of rs-fMRI BOLD signals and brain amyloid deposition measured with PET AV45-SUVR in regions associated with default-mode and visual networks in aMCI patients. We have also shown that stepwise removal



**Figure 4.** Impact of stepwise regression of upper-stream vascular effects on the correlations between brain amyloid- $\beta$  deposition and the amplitude of low-frequency BOLD signal fluctuations (sALFF) in the significant clusters identified with “no physiological regression” (a) and “aggressive AROMA” (b). Stars on brackets denote significance levels of paired Mann-Whitney U-tests with  $*p \leq 0.05$ ,  $**p \leq 0.01$ ,  $***p \leq 0.001$ . Fisher z transformed  $r$ -value distributions shown in violin plots: (a) Using the  $r$ -values of all voxels within the significant clusters reported in Table 2 under “no physiological regression”. This comparison shows a stepwise decrease of negative correlation magnitude as more aggressive physiological signal removal procedures were applied, suggesting that BOLD-fluctuations at these voxel locations are more driven by upper-stream vascular effects; (b) Using the  $r$ -values of all voxels within the significant clusters reported in Table 2 under “aggressive AROMA”. This comparison shows a stepwise increase of negative correlation magnitude as more aggressive physiological signal removal procedures were applied, suggesting that BOLD fluctuations at these voxel locations are more likely driven by neuronal activity.

of the upper-stream physiological/vascular signals reduced the correlation strength between sALFF and AV45-SUVr at these regions. However, even the most intensive upper-stream physiological/vascular signal regression procedures implemented in this study did not completely abolish the negative correlations between sALFF and AV45-SUVr in regions associated with default-mode and visual networks. These findings suggest low-frequency upper-stream cerebral arterial pressure, as well as blood flow fluctuations, are transmitted into the cerebral microcirculation, where they may play an important role in brain A $\beta$  deposition.<sup>35</sup> Conversely, our data also support the hypothesis that local neuronal activity fluctuations contribute to A $\beta$  homeostasis, independent of the upper-stream vascular effect.

Further evidence of the anti-correlative relationship between fMRI fluctuation amplitude and A $\beta$  deposition was given by our correlation analyses between sALFF and AV45-SUVr within each subject brain, across the 116 AAL brain regions for each regression procedure. We found the correlation strength between sALFF and AV45-SUVr was reduced as more cardiovascular signals were regressed out. This finding demonstrated a significant effect of cardiovascular regression on this correlation. Even after the most

stringent aggressive AROMA regression procedure, a significant within-brain anti-correlation between sALFF and AV45-SUVr remained. As all within-brain correlations were significantly negative, we can interpret that globally, high BOLD fluctuations are associated with low A $\beta$  deposition and vice versa. This relationship was strongest when no cardiovascular regression was performed, implying a strong cardiovascular contribution to A $\beta$  deposition while not being its sole determinant.

Furthermore, supplementary data analyses revealed trends for lower sALFF, higher AV45-SUVr and stronger anti-correlation between sALFF and AV45-SUVr for APOE4 carriers (see Supplementary Material). Below, we discuss the potential mechanisms and methodological considerations.

### Potential mechanisms

Brain metabolic waste products, including A $\beta$ , are cleared partly via the recently identified brain glymphatic system.<sup>13,64</sup> This system is a highly organized brain metabolite transportation system between brain interstitial fluid (ISF), cerebrospinal fluid (CSF), and the cerebral vasculature.<sup>13,64</sup> One theory proposed that CSF enters the perivascular spaces from the

subarachnoid space and is propelled deep into the brain by arterial pulsatility. The CSF subsequently enters the neuropil via the astrocytes AQP4 water channels. It then mixes with brain ISF in the extracellular space and leaves the brain, along with brain waste products via the perivenous space into the systemic glymphatic system.<sup>13</sup> Conversely, other studies have shown that brain waste products also can be cleared via backflow through the periarterial basement space.<sup>64</sup> Regardless of specific vascular clearance pathways, cerebral arterial pulsatility has been proposed as a key driver of brain waste clearance through these pathways.<sup>14</sup> Furthermore, a recent study showed that spontaneous cerebral arteriolar vasomotion at a frequency of  $\sim 0.1$  Hz was correlated with paravascular clearance of A $\beta$  in awake mouse brains (van Veluw et al. *Neuron* 2020), while MRI studies also suggest that low-frequency waves in the CSF of  $\sim 0.02$  and  $\sim 0.05$  Hz are likely related to brain A $\beta$  clearance.<sup>65,66</sup> In this regard, our previous study has demonstrated that brain BOLD signal fluctuations at the regions associated with the default-mode and the visual networks have similar spectral distribution to the fluctuations of systemic blood pressure and CBF velocity measured from the middle cerebral artery, suggesting these upstream vascular signals may transmit downstream into the cerebral microcirculation and impact A $\beta$  clearance.<sup>35</sup>

The present study extended these previous studies by showing that significant negative correlations exist between spontaneous low-frequency BOLD fluctuations and brain amyloid deposition, measured using PET AV45-SUVR, in default-mode and visual networks in aMCI patients. These findings taken together with the previous studies discussed above suggest that hemodynamic fluctuations transmitted from the upper-stream cardiovascular and cerebrovascular systems into the cerebral microcirculation may influence A $\beta$  homeostasis in individuals with elevated risk for AD. Consistent with this hypothesis, we have found that age-related carotid artery stiffness was associated positively with brain A $\beta$  burden in aMCI patients, suggesting cerebral arterial stiffening may attenuate the transmission of arterial pressure and blood flow oscillations into the brain, leading to a reduction of brain amyloid clearance.<sup>11,67</sup>

Interestingly, even with the most intensive upper-stream physiological/vascular signal removal procedure implemented in this study, negative correlations between sALFF and AV45-SUVR were still present in default-mode and visual regions. These findings suggest that local neuronal activity fluctuations might also prevent brain A $\beta$  deposition.

### Methodological considerations

For calculating the PET AV45-SUVR, we chose white matter (WM) instead of the more traditional cerebellum as the reference for normalization. The comparison between reference regions has been comprehensively discussed by Brendel et al.<sup>61</sup> Nevertheless, we repeated our analyses with the cerebellum as the reference for AV45-SUVR calculation, finding the same trend of negative correlation between local sALFF and AV45-SUVR. See Supplementary Material for a detailed discussion regarding the reference for AV45-SUVR calculation.

The mean sALFF images in Figures 2 and S6 show a strong preprocessing effect. As more and more global variance is removed through the different regression procedures, the normalization of ALFF to sALFF can reveal changes in local fluctuations. The different noise regression models all had inherent motion confound modeling, yet the amount of physiological/vascular regression varied. While WM and cerebrospinal fluid (CSF) signals are widely accepted to represent physiological/vascular signal components,<sup>55</sup> the much-debated global signal has recently been shown to also represent a substantial amount of physiological/vascular signals.<sup>56,68</sup> The data-driven “ICA-AROMA” approach creates noise-regressors that are closely tailored to the data,<sup>59</sup> making it the most demanding regression model in this study.

### Limitations and strengths

Only 33 aMCI participants were available for this study and thus the statistical power for voxel-wise analyses was limited. In addition, no healthy controls were available to study a broader range of populations. However, our voxel-wise analyses have clearly shown an anti-correlation between sALFF and AV45-SUVR. Changes in the correlation strength due to different regression procedures were further presented with cluster-based correlation analyses. However, a causal relationship between brain A $\beta$  deposition and BOLD fluctuation quantified by ALFF cannot be determined from this preliminary cross-sectional investigation.

The discriminative power of AV45 imaging in AD has been proven in many studies, nonetheless, there are limitations.<sup>69</sup> PET images inherently contain a high level of spatial blurring, in addition to a relatively low spatial resolution provided by signal detection. Additionally, the high level of non-specific binding to white matter leads to segmentation and registration inaccuracies at the border between gray and white matter.<sup>70</sup> Especially in the situation of grey matter atrophy, commonly observed in AD, the signal at the cortical grey matter is inevitably contaminated by white

matter signal, resulting in reduced specificity. Using the advanced FreeSurfer segmentation from the anatomical MRI recordings, paired with the manually supervised alignment of AV45 PET images to the anatomical images, we can reduce these segmentation issues in AV45 PET images.

The challenging step of normalizing brains of a study population with pronounced atrophy and ventricle enlargement into a common space was mostly overcome using the FreeSurfer based non-linear transformation. Visual assessment confirmed good normalization results for cortical areas, only some subcortical and white matter areas suffered from non-linear stretching artifacts. However, all reported results are within the cortical regions. Nonetheless, the minor normalization artifacts of subcortical and WM regions might have contributed to false negative results in the subcortical regions.

RS-fMRI with a high sampling rate, such as the 0.1 s TR used by Raitamaa and colleagues,<sup>71</sup> might have been more suited for frequency spectrum-based analyses of cardiovascular signals within fMRI data. The relatively long TR of 1.5 s in our rs-fMRI data placed limitations on frequency spectrum-based analyses due to the aliasing of cardiac signals and potentially respiratory signals as well. Nonetheless, even with these restrictions, employing the presented differential regression procedures allows us to at least partially overcome these limitations and approximate the cardiovascular signals for the aim of this study. In addition to motion derived residuals, the regressors employed in this study represent cardiovascular signals to a varying degree: CSF and WM signals should not contain neurovascular reactivity and thus represent mainly the effects of respiratory and cardiovascular pulsatility and their respective aliases and harmonics within the typical neurovascular frequency band.<sup>56</sup> Furthermore, Xifra-Porxas et al.<sup>56</sup> showed that about 60% of the global mean signal are represented by upper-stream cardiovascular effects, thus making it a suitable regressor, even though it bears the risk of partially removing signals from neurovascular activity. The aggressive AROMA regression, as the most stringent regression procedure, finds a spatially independent decomposition of the data and classifies each component as either a noise related or not noise related component. Noise related components in AROMA are classified based on their resemblance of cardiovascular, respiratory, motion, high-frequency, and other structured noises in the data. Components that were classified as noise were subsequently regressed from the data. As these regressors were directly defined by the data, the assumption was that after the aggressive AROMA procedure, the remainder resembles neurovascular activity related signals with random noise.

Concerning the model order of the respective regression procedure, aggressive AROMA has the highest number of regressors.

With only seven of 33 subjects carrying the APOE4 gene, statistical analyses regarding genotype were underpowered and thus could only show trends (see Supplementary Material). However, these trends are very promising and warrant further studies with larger sample sizes.

## Conclusions

This study has shown that local spontaneous BOLD signal fluctuations are negatively associated with brain A $\beta$  accumulation measured with amyloid PET in aMCI subjects who are at a high risk for AD. Furthermore, we found that physiological signal regression decreased the cluster size of negative correlations between low-frequency BOLD signal fluctuation and PET AV45-SUV<sub>R</sub>. Nevertheless, the most intensive physiological/vascular regression procedures did not completely abolish the correlations between BOLD signal fluctuations and PET AV45-SUV<sub>R</sub>. Therefore, these findings collectively suggest that both cerebral hemodynamic fluctuations and local neuronal activity play important roles in brain A $\beta$  homeostasis in older adults with aMCI.

## Funding

The author(s) disclosed receipt of the following financial support for the research, authorship, and/or publication of this article: Funding towards this work was received from the National Institutes of Health (R01AG033106, R01HL102457, and R01AG057571).

## Acknowledgements

We thank each of the study participants for their effort and time contributing to the study. The <sup>18</sup>F-florbetapir PET radiotracer was provided to the study by Avid Radiopharmaceuticals.

## Declaration of conflicting interests

The author(s) declared no potential conflicts of interest with respect to the research, authorship, and/or publication of this article.


## Authors' contributions

N. Scheel performed data analysis, drafted and finalized the manuscript. T. Tarumi participated in data collection, data analysis, and manuscript writing/editing. T. Tomoto participated in data collection and manuscript writing/editing. C. M. Cullum provided clinical neuropsychological input and manuscript writing/editing. R. Zhang developed concepts and participated in manuscript writing/editing. D. C. Zhu developed concepts and participated in data analysis and manuscript writing/editing. All authors contributed

intellectually to conceive this work, revised, and approved the final version of the manuscript.

### ORCID iDs

Norman Scheel  <https://orcid.org/0000-0002-4641-7579>

Tsubasa Tomoto  <https://orcid.org/0000-0001-5936-0332>

### Supplemental material

Supplemental material for this article is available online.

### References

1. Matthews KA, Xu W, Gaglioti AH, et al. Racial and ethnic estimates of Alzheimer's disease and related dementias in the United States (2015–2060) in adults aged  $\geq 65$  years. *Alzheimers Dement* 2019; 15: 17–24.
2. McKhann GM, Knopman DS, Chertkow H, et al. The diagnosis of dementia due to Alzheimer's disease: Recommendations from the national institute on Aging-Alzheimer's association workgroups on diagnostic guidelines for Alzheimer's disease. *Alzheimers Dement* 2011; 7: 263–269.
3. Querfurth HW and LaFerla FM. Alzheimer's disease. *N Engl J Med* 2010; 362: 329–344.
4. Petersen RC, Lopez O, Armstrong MJ, et al. Practice guideline update summary: mild cognitive impairment report of the guideline development, dissemination, and implementation. *Neurology* 2018; 90: 126–135.
5. Hardy JA and Higgins GA. Alzheimer's disease: the amyloid cascade hypothesis. *Science* 1992; 256: 184–185.
6. De la Torre JC and Mussivand T. Can disturbed brain microcirculation cause Alzheimer's disease? *Neurol Res* 1993; 15: 146–153.
7. de la Torre J. The vascular hypothesis of Alzheimer's disease: a key to preclinical prediction of dementia using neuroimaging. *J Alzheimers Dis* 2018; 63: 35–52.
8. Iadecola C, Duering M, Hachinski V, et al. Vascular cognitive impairment and dementia: JACC scientific expert panel. *J Am Coll Cardiol* 2019; 73: 3326–3344.
9. Gaugler J, James B, Johnson T, et al. Alzheimer's disease facts and figures. *Alzheimer's Dement* 2016 2016; 12: 459–509.
10. Jack CR, Bennett DA, Blennow K, Contributors, et al. NIA-AA research framework: toward a biological definition of Alzheimer's disease. *Alzheimers Dement* 2018; 14: 535–562.
11. Pasha EP, Rutjes E, Tomoto T, et al. Carotid stiffness is associated with brain amyloid- $\beta$  burden in amnesic mild cognitive impairment. *J Alzheimers Dis* 2020; 74: 925–935.
12. van Veluw SJ, Hou SS, Calvo-Rodriguez M, et al. Vasomotion as a driving force for paravascular clearance in the awake mouse brain. *Neuron* 2020; 105: 549–561.e5.
13. Nedergaard M and Goldman SA. Glymphatic failure as a final common pathway to dementia. *Science* 2020; 370: 50–56.
14. Iliff JJ, Wang M, Zeppenfeld DM, et al. Cerebral arterial pulsation drives paravascular CSF-Interstitial fluid exchange in the murine brain. *J Neurosci* 2013; 33: 18190–18199.
15. Biswal B, Yetkin FZ, Haughton VM, et al. Functional connectivity in the motor cortex of resting human brain using echo-planar MRI. *Magn Reson Med* 1995; 34: 537–541.
16. Fox MD and Raichle ME. Spontaneous fluctuations in brain activity observed with functional magnetic resonance imaging. *Nat Rev Neurosci* 2007; 8: 700–711. Epub ahead of print DOI: 10.1038/nrn2201.
17. Heeger DJ and Ress D. What does fMRI tell us about neuronal activity? *Nat Rev Neurosci* 2002; 3: 142–151.
18. Greicius MD, Krasnow B, Reiss AL, et al. Functional connectivity in the resting brain: a network analysis of the default mode hypothesis. *Proc Natl Acad Sci U S A* 2003; 100: 253–258.
19. Greicius MD, Supekar K, Menon V, et al. Resting-state functional connectivity reflects structural connectivity in the default mode network. *Cereb Cortex* 2009; 19: 72–78.
20. Johnston JM, Vaishnavi SN, Smyth MD, et al. Loss of resting interhemispheric functional connectivity after complete section of the corpus callosum. *J Neurosci* 2008; 28: 6453–6458.
21. Ebisch SJH, Gallese V, Willems RM, et al. Altered intrinsic functional connectivity of anterior and posterior insula regions in high-functioning participants with autism spectrum disorder. *Hum Brain Mapp* 2011; 32: 1013–1028.
22. Fair DA, Posner J, Nagel BJ, et al. Atypical default network connectivity in youth with attention-deficit/hyperactivity disorder. *Biol Psychiatry* 2010; 68: 1084–1091.
23. Baudrexel S, Witte T, Seifried C, et al. Resting state fMRI reveals increased subthalamic nucleus-motor cortex connectivity in parkinson's disease. *Neuroimage* 2011; 55: 1728–1738.
24. Chen G, Ward BD, Xie C, et al. Classification of AD, MCI, and NC status with large-scale network analysis based on rs-fMRI. *Radiology* 2011; 259: 213–221.
25. Park CH, Chang WH, Ohn SH, et al. Longitudinal changes of resting-state functional connectivity during motor recovery after stroke. *Stroke* 2011; 42: 1357–1362.
26. Zhu DC, Majumdar S, Korolev IO, et al. Alzheimer's disease and amnesic mild cognitive impairment weaken connections within the default-mode network: a multimodal imaging study. *J Alzheimers Dis* 2013; 34: 969–984.
27. Raichle ME and Mintun MA. Brain work and brain imaging. *Annu Rev Neurosci* 2006; 29: 449–476.
28. Shmueli K, van Gelderen P, de Zwart J, et al. Low-frequency fluctuations in the cardiac rate as a source of variance in the resting-state fMRI BOLD signal. *Neuroimage* 2007; 38: 306–320.
29. Chang C, Cunningham JP and Glover GH. Influence of heart rate on the BOLD signal: the cardiac response function. *Neuroimage* 2009; 44: 857–869.
30. Chang C and Glover GH. Time-frequency dynamics of resting-state brain connectivity measured with fMRI. *Neuroimage* 2010; 50: 81–98.

31. Chang C, Metzger CD, Glover GH, et al. Association between heart rate variability and fluctuations in resting-state functional connectivity. *Neuroimage* 2013; 68: 93–104.
32. Tsvetanov KA, Henson RNA, Jones PS, et al. The effects of age on resting-state BOLD signal variability is explained by cardiovascular and cerebrovascular factors. *Psychophysiology* 2020; : 1–20.
33. Rajna Z, Raitamaa L, Tuovinen T, et al. 3D multi-resolution optical flow analysis of cardiovascular pulse propagation in human brain. *IEEE Trans Med Imaging* 2019; 38: 2028–2036.
34. Rajna Z, Mattila H, Huotari N, et al. Cardiovascular brain impulses in Alzheimer's disease. *Brain* 2021; 144: 2214–2226.
35. Zhu DC, Tarumi T, Khan MA, et al. Vascular coupling in resting-state fMRI: evidence from multiple modalities. *J Cereb Blood Flow Metab* 2015; 35: 1910–1920.
36. Sperling RA, Laviolette PS, O'Keefe K, et al. Amyloid deposition is associated with impaired default network function in older persons without dementia. *Neuron* 2009; 63: 178–188.
37. Makedonov I, Chen JJ, Masellis M, et al. Physiological fluctuations in white matter are increased in Alzheimer's disease and correlate with neuroimaging and cognitive biomarkers. *Neurobiol Aging* 2016; 37: 12–18.
38. Scarapicchia V, Mazerolle EL, Fisk JD, et al. Resting state BOLD variability in Alzheimer's disease: a marker of cognitive decline or cerebrovascular status? *Front Aging Neurosci* 2018; 10: 1–13.
39. Tuovinen T, Kananen J, Rajna Z, et al. The variability of functional MRI brain signal increases in Alzheimer's disease at cardiorespiratory frequencies. *Sci Rep* 2020; 10: 1–11.
40. Zang YF, Yong H, Chao-Zhe Z, et al. Altered baseline brain activity in children with ADHD revealed by resting-state functional MRI. *Brain Dev* 2007; 29: 83–91.
41. Pruim RHR, Mennes M, van Rooij D, et al. Ica-AROMA: a robust Ica-based strategy for removing motion artifact from fMRI data. *Neuroimage* 2015; 112: 267–277. Epub ahead of print DOI: 10.1016/j.neuroimage.2015.02.064.
42. Caballero-Gaudes C and Reynolds RC. Methods for cleaning the BOLD fMRI signal. *Neuroimage* 2017; 154: 128–121.
43. Poline J-B and Brett M. The general linear model and fMRI: does love last forever? *Neuroimage* 2012; 62: 871–880.
44. Tarumi T, Rossetti H, Thomas BP, et al. Exercise training in amnesic mild cognitive impairment: a one-year randomized controlled trial. *J Alzheimers Dis* 2019; 71: 421–433.
45. Petersen RC, Smith GE, Waring SC, et al. Mild cognitive impairment: clinical characterization and outcome. *Arch Neurol* 1999; 56: 303–308.
46. Morris JC. The clinical dementia rating (CDR): current version and scoring rules. *Neurology* 1993; 43: 2412–2414.
47. Folstein MF, Folstein SE and McHugh PR. 'Mini-mental state': a practical method for grading the cognitive state of patients for the clinician. *J Psychiatr Res* 1975; 12: 189–198.
48. Wechsler D. *Wechsler memory scale-revised: manual*. San Antonio, TX: Psychological Corporation, 1987.
49. Clark CM, Schneider JA, Bedell BJ, et al. Use of florbetapir-PET for imaging  $\beta$ -amyloid pathology. *JAMA – J Am Med Assoc* 2011; 305: 275–283.
50. Rodrigue KM, Kennedy KM, Devous MD, et al.  $\beta$ -amyloid burden in healthy aging: regional distribution and cognitive consequences. *Neurology* 2012; 78: 387–395.
51. Chao-Gan Y and Yu-Feng Z. DPARSF: a MATLAB toolbox for pipeline data analysis of resting-state fMRI. *Front Syst Neurosci* 2010; 4: 13.
52. Yan CG, Wang X, Di Zuo XN, et al. DPABI: Data processing & analysis for (resting-state) brain imaging. *Neuroinformatics* 2016; 14: 339–351.
53. Fischl B, Salat DH, Busa E, et al. Whole brain segmentation: automated labeling of neuroanatomical structures in the human brain. *Neuron* 2002; 33: 341–355.
54. Cox JSRH. AFNI: Software for analysis and visualization of functional magnetic resonance neuroimages. *Comput Biomed Res* 1996; 29: 162–173.
55. Fox MD, Snyder AZ, Vincent JL, et al. The human brain is intrinsically organized into dynamic, anticorrelated functional networks. *Proc Natl Acad Sci U S A* 2005; 102: 9673–9678.
56. Xifra-Porxas A, Kassinopoulos M and Mitsis GD. Physiological and motion signatures in static and time-varying functional connectivity and their subject identifiability. *Elife* 2021; 10: 1–36.
57. Kassinopoulos M and Mitsis GD. Identification of physiological response functions to correct for fluctuations in resting-state fMRI related to heart rate and respiration. *Neuroimage* 2019; 202: 116150.
58. Kassinopoulos M and Mitsis GD. White matter denoising improves the identifiability of large-scale networks and reduces the effects of motion in fMRI functional connectivity. *bioRxiv* 2020: 837609.
59. Pruim RHR, Mennes M, Buitelaar JK, et al. Evaluation of Ica-AROMA and alternative strategies for motion artifact removal in resting-state fMRI. *Neuroimage* 2015; 112: 278–287. Epub ahead of print DOI: 10.1016/j.neuroimage.2015.02.063.
60. Jenkinson M, Beckmann CF, Behrens TEJ, et al. FSL. *Neuroimage* 2012; 62: 782–790.
61. Brendel M, Högenauer M, Delker A, Alzheimer's Disease Neuroimaging Initiative, et al. Improved longitudinal [18F]-AV45 amyloid PET by white matter reference and VOI-based partial volume effect correction. *Neuroimage* 2015; 108: 450–459.
62. Golland P, Liang F, Mukherjee S, et al. Permutation tests for classification. *Learn Theory* 2005; 1: 1–22.
63. Tzourio-Mazoyer N, Landeau B, Papathanassiou D, et al. Automated anatomical labeling of activations in SPM using a macroscopic anatomical parcellation of the MNI MRI single-subject brain. *Neuroimage* 2002; 15: 273–289.
64. Weller RO, Hawkes CA, Kalaria RN, et al. White matter changes in dementia: Role of impaired drainage of interstitial fluid. *Brain Pathol* 2015; 25: 63–78.

65. Kiviniemi V, Wang X, Korhonen V, et al. Ultra-fast magnetic resonance encephalography of physiological brain activity-Glymphatic pulsation mechanisms? *J Cereb Blood Flow Metab* 2016; 36: 1033–1045.
66. Fultz NE, Bonmassar G, Setsompop K, et al. Coupled electrophysiological, hemodynamic, and cerebrospinal fluid oscillations in human sleep. *Science* 2019; 366: 628–631.
67. Sugawara J, Tarumi T, Xing C, et al. Older age and male sex are associated with higher cerebrovascular impedance. *J Appl Physiol* 2020. Epub ahead of print DOI: 10.1152/jappphysiol.00396.2020.
68. Murphy K, Birn RM, Handwerker D. a, et al. The impact of global signal regression on resting state correlations: are anti-correlated networks introduced? *Neuroimage* 2009; 44: 893–905.
69. Saint-Aubert L, Barbeau EJ, Péran P, et al. Cortical florbetapir-PET amyloid load in prodromal Alzheimer's disease patients. *EJNMMI Res* 2013; 3: 43–22.
70. Wolk DA, Zhang Z, Boudhar S, et al. Amyloid imaging in Alzheimer's disease: comparison of florbetapir and pittsburgh compound-B positron emission tomography. *J Neurol Neurosurg Psychiatry* 2012; 83: 923–926.
71. Raitamaa L, Huotari N, Korhonen V, et al. Spectral analysis of physiological brain pulsations affecting the BOLD signal. *Hum Brain Mapp* 2021; 42: 4298–4313.